Spin-Controlled Helical Quantum Sieve Chiral Spectrometer

*Arnab Maity, Yael Hershkovitz-Pollak, Ritu Gupta, Weiwei Wu, and Hossam Haick**

This article reports on a molecular-spin-sensitive-antenna (MSSA) that is based on stacked layers of organically functionalized graphene on a fibrous helical cellulose network for carrying out spatiotemporal identification of chiral enantiomers. The MSSA structures combine three complementary features: (i) chiral separation via a helical quantum sieve for chiral trapping, (ii) chiral recognition by a synthetically implanted spin-sensitive center in a graphitic lattice; and (iii) chiral selectivity by a chirality-induced-spin mechanism that polarizes the local electronic band-structure in graphene through chiral-activated Rashba spin–orbit interaction field. Combining the MSSA structures with decision-making principles based on neuromorphic artificial intelligence shows fast, portable, and wearable spectrometry for the detection and classification of pure and a mixture of chiral molecules, such as butanol (S and R), limonene (S and R), and xylene isomers, with 95–98% accuracy. These results can have a broad impact where the MSSA approach is central as a precautionary risk assessment against potential hazards impacting human health and the environment due to chiral molecules; furthermore, it acts as a dynamic monitoring tool of all parts of the chiral molecule life cycles.

1. Introduction

Chirality is a property of molecules that results in their mirror images being non-superimposable, even with any translation or rotation.[1] This property arise when a molecule has an asymmetric carbon atom or other chiral center, which creates two mirror image structures known as enantiomers. Chiral molecules have identical physical and chemical properties when present in an achiral environment.[2] Due to their essential role in various chemical and biological processes, the determination of absolute configuration and enantiopurity is crucially important in a whole range of fields, such as biosensing, optics, electronics, photonics, catalysis, nanotechnology, and drug and DNA delivery; notably it is crucially important in drug production and the material sciences.[3]

Several approaches have made significant progress over the last few years for chiral detection methods.[4–10] These include chromatographic separation, optical polarization, and sieving techniques, such as, supercritical fluid chromatography using a polysaccharide-based stationary-phase, optoelectronics-based polarizer instruments (e.g., circular dichroism spectroscopy), and a porous organic cage.[4–10]

However, these instruments are bulky, expensive, power-hungry, need tedious fabrication and production methods, and require long processing time with stringent analyses by trained people.

At the front of the aforementioned challenges, sensors with various transduction mechanisms (e.g., chemiresistor, photoconductive, and field effect transistors) have been proposed for rapid, continuous, automated, and/or on-site precautionary risk assessments for potential chiral hazards impacting human health and the environment, and/or for the dynamic monitoring of all parts of the chiral molecule life-cycles.[11–16] Amongst the reported sensing approaches, enantioselective chemical microsensors based on helical structures, such as DNA, have also been proposed for investigating extra-terrestrial homochirality in space.[17] For these structures, efficient sensing performance relies on the energetically favorable binding of a specific enantiomer type to the helical structure through two-point or three-point interaction; at the time the other enantiomer has less favorable binding energy on the same helical structure. While good performances have been reported with this approach, this strategy is not so effective in evaluating chiral mixtures because in most of the cases, the sensor device provides a superposed signal from a chiral mixture and lacks chiral separation.[11,14] Indeed, for the detection and classification of chiral mixture combinations, the use of these superimposed signals requires tiresome training of an uncountable combination of sensing signals.[18]

To monitor the life cycle of each chiral molecule and pinpoint potential new chemical threats, it is first necessary to detect and

A. Maity, Y. Hershkovitz-Pollak, H. Haick
Department of Chemical Engineering and Russell
Berrie Nanotechnology Institute
Technion – Israel Institute of Technology
Haifa 3200003, Israel
E-mail: hhossam@technion.ac.il
R. Gupta
Department of Chemistry
Indian Institute of Technology Jodhpur
Jodhpur, Rajasthan 342037, India
W. Wu, H. Haick
School of Advanced Materials and Nanotechnology
Xidian University
Xi'an, Shaanxi 710126, P. R. China

**ADVANCED
SCIENCE NEWS**

www.advancedsciencenews.com

**ADVANCED
MATERIALS**

www.advmat.de

identify ideally all, or at least most, chiral compounds within the targeted environment or mixture. An ideal chiral sensor that could achieve this target demands four complementary characteristics: (i) it can strongly interact with chiral molecules so that it can detect the analytes at low concentrations; (ii) energetically favorable binding can induce strong responses and differentiate a pair of enantiomers with high sensitivity; (iii) the chirality induction is real-time and can be measured directly without after-treatment; and (iv) the molecular host is easier to synthesize and chemically modify. One approach that could achieve these characteristics relies on advanced materials and geometrical structures that have the ability of producing opposite spin information from each chiral handedness. This property is commonly known as chirality-induced spin selectivity (CISS)[19,20] which could be practically initiated as an asymmetric electron-scattering process in a chiral potential, dependent on spin–orbit interactions (SOI).[21–25] Essentially, spin adds new degrees of freedom for the conventional sensing approach. Its manifestation as a major recognizing factor for a chiral molecule to be established as a prominent transduction principle remains to be achieved.

We report here on the design and demonstration of a chiral spectrometer that can simultaneously separate and detect vapor mixtures of enantiomers. The detection ability of this chiral spectrometer is based on the chirality-assisted spin-control principle using spin-sensitive and spin-selective hybrid graphene pixels printed on a helical quantum sieve (HQS)-based cellulose structure with a cascaded architecture. By engineering a cascade of porous and hairy HQS networks as a Chiral Stationary Phases (CSP), it is possible to obtain the separation for mixtures of chiral molecules, through a spatiotemporal effect that binds and releases the chiral handedness of the molecules in diverse times and places. This detection and classification mechanism is examined and supported by: (i) molecular modeling for calculating the binding energy of the various components of paper (such as cellulose) with the enantiomers and isomers as well as the asymmetry in energy and relapsing time for each component in the targeted chiral mixture; and (ii) quantum mechanical study with density functional theory (DFT) calculation for evaluating the energy of interaction of chiral molecule-organic ligands of sensor and spin influence on band structure. For application purposes, a neuromorphic vision-inspired image-processing technique along with a deep neural network base is used to assess pure and mixture of target enantiomers/isomers qualitatively and quantitatively.

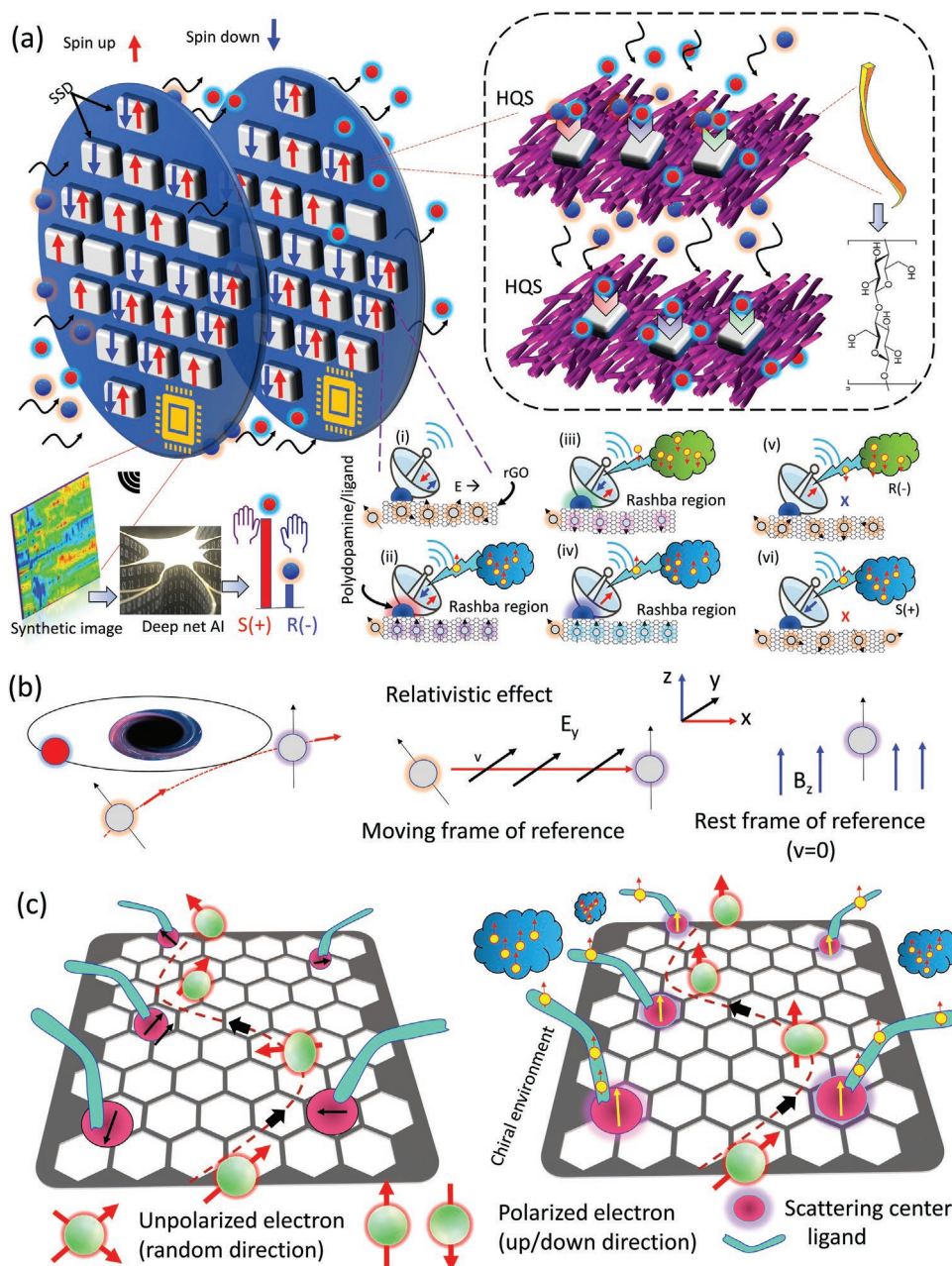## 2. Design of Chiral Sensitive Electronic Architecture on Helical Quantum Sieve

Figure 1a presents the overall design structure of the spatiotemporal-based chiral spectrometer, which relies on chiral sensitive electronic architecture on helical quantum sieve (CSEAHQS) in cascaded layers. Each layer within the CSEAHQS consists of a variety of spin-sensitive detectors (SSDs) that are made of different molecular-spin-sensitive-antenna (MSSA) receptors (chiral/achiral) grafted on to a graphite plane (see Section S1, Supporting Information) and operated by CISS. Thus, CISS-pumped electrons polarize the conductive graphitic framework

to certain spin states via MSSA, and such adatom creates Rashba, a SOI field as their presence breaks the space inversion symmetry.[22–25] Due to the presence of multiple SSDs in each layer of the CSEAHQS, a splitting phenomenon for each SSD could be viewed simultaneously and in a multiplexed manner, providing classification/quantification of individual or mixture of chiral molecules using synthetic image processing (see below). The inset of Figure 1a shows the magnified schematic of the printed SSD on helical cellulose like fiber structures (HQS). While the measured sensing signal in the top cascade layer is a superimposition of both types of chiral molecules, it is likely that signal from second cascade layer will show a spatiotemporal chiral separation (resolving power) due to helical interaction of cellulose and each enantiomers).

Figure 1a[i–vi] shows the schematics of the channel polarization from the enantiomer's spin injection via the implanted scattering center, expressed via a dopamine ligand that is chemically attached to the graphite surface. Also shown is the unpolarized electron injected from the lead to the channel to gain more uniform polarizability due to the implanted scattering center while passing through the Rashba region—a region that is influenced by a certain spin state as destined by type of the chiral molecule as well as the efficiency/quality of spin transfer through the ligands. The advantage of weak spin–orbit and hyperfine interactions in the organic ligands helps in preserving spin-coherence over time and distance, which are much longer ($\approx$13–110 nm) than conventional metals.[26–29] As such, tuning the grafted organic ligands on the graphite plane of the MSSA can act either as a coherent spin channel or as a spin filter.

A special spin polarization originating from certain chiral molecules can be transported through organic linkers to a graphite-based channel. Depending on the handedness, this can cause opposing change in resistance. This capability to distinguish different spin directions, known as 'spin filter', results in a specific spin type being accepted while the other spin is not. In the "spin filter" case, specific spin (viz. up) is selectively transferred to the channel and remains opaque for the other spin type (viz. down). The result is chiral selectivity expressed by a change in the resistance (increase/decrease) for one specific enantiomer and silence for its mirror type (see Figure 1a[i–vi]). Relevant to this case is the adatom of the organic ligand implanted on the graphite lattice that act as a scattering source for precessing the incoming electron spin, as per Rashba field direction (Dyakonov–Perel type) or local magnetic moment influence (resonant scattering type) – see Figure 1b,c. On exposure to enantiomeric vapor molecules, these scattering regions indicate the same direction of the Rashba field and magnetic moment throughout the entire exposed area of SSD, creating a strong spin polarization effect from local counterpoints to globally across the SSD. This effect is termed throughout this article as "chiral activated Rashba effect" (CARE).

The Rashba SOI effect is empowered when a scattering center is spin-polarized by the chiral environment (CARE phenomena) and a spin-polarized band gap is modulated in the presence of such heavier dopant that radically changes the local electronic structure (see Figure 1b,c). In the presence of electric field in the same direction, where inversion symmetry is broken, $\boldsymbol{E}$ (= E $\hat{z}$), a moving electron with a velocity $\boldsymbol{v}$ experiences a relativistic

**ADVANCED
SCIENCE NEWS**

www.advancedsciencenews.com

**ADVANCED
MATERIALS**

www.advmat.de

Figure 1. Spin-controlled chiral spectrometer using the relativistic chiral Rashba effect, MSSA, and HQS as chiral stationary phase. a) CSEAHQS architecture based on chiral spin spectrometer with embedded signal processing unit and deep net-based decision-making system using synthetic image processing from the feedback of SSDs. The arrows (up–down, up, down, and no symbol) signify the operating mode of the detectors that can sense up and down, up, down, and no spin type, respectively, depending on the functionalization status around the graphite plane. The HQS structure is shown in the dotted inset. The Rashba SOI region and CISS-based spin transfer from chiral molecules adsorb on such MSSA is shown for polarization of the channel and compared with various cases, such as (i) without enantiomers vapor (negligible polarization), with enantiomer, for (ii) spin-up, and (iii) the spin-down polarization case, where MSSA transfers both spin-type coherently. MSSA is tuned for spin filter to allow (iv) specific spin (such as up) that detect specific enantiomer by polarizing the channel selectively, and (v,vi) opaque for other spin types (defined as "x") that have negligible influence in channel polarization and have an insignificant resistance change that leads to chiral selectivity. b) Relativistic representation of moving spinning electron and polarization by SOI is considered in the observer's moving/rest frame of reference for the direction of moving electrons (v), electric (E_y), and magnetic field (B_z). c) Schematic comparison of two cases showing chiral Rashba SOI for polarization of electron flow without (left) and with (right) enantiomer in a 2D SSD system.

effective magnetic field B. Therefore, Zeeman influence on the electron takes the form of the Rashba SOI, as expressed by:

$$H_{\text{zeman}} = -eh / 2m (\sigma . B) = -\alpha_z (\sigma \times k) . \hat{z} \quad (1)$$

**ADVANCED
SCIENCE NEWS**

www.advancedsciencenews.com

**ADVANCED
MATERIALS**

www.advmat.de

where $\alpha_z = (\hbar/mc)^2 \, eE/2$ gives the Rashba energy scale and σ and k are electron's spin and crystal momentum, respectively (see details in Section S2, Supporting Information). This arises from the inherent magnetic field due to a relativistic effect, which is the key factor for spin polarization without an external field. This relativistic effect is advantageous over other magnetic resonance spectroscopy, such as electron spin resonance (ESR) and nuclear magnetic resonance (NMR), where an external magnetic field is needed to generate the electron spin energy band splitting and the radio frequency scanning to identify them.

2.1. Synthesis and Printing SSDs on HQS

Printing the SSDs is carried out by the binder-free inkjet technique using dopamine-assisted reduction of graphene oxide (GO) functionalized with molecular spin sensitive antenna, expressed by various chiral and achiral biochemical ligands (see Figure S1 and Section S1, Supporting Information). The advantage of the implemented binder-free printing technique is that it does not need any post-printing annealing, making it suitable for high-quality printing on wide range flexible/rigid and porous substrates (e.g., paper, Kapton, glass, PDMS polymers, and PET)—see **Figure 2**a–j.

Figure 2k shows typical scanning electron microscopy (SEM) of reduced GO (rGO) nano-flex after reduction. The details of the chiral/achiral biochemical ligand are given in Figure S1, Supporting Information. The functionalized-rGO inks are printed in a multijunction array electrode on a porous paper substrate that acts as HQS. Figure 2l shows an optical image of a representative CSEAHQS, in which the 20 black pixels represent various functionalized-rGO detectors and the gray lines represent the silver nanowire-based electrodes and connectors. Figure 2m shows the Raman spectroscopy measurement and the calculated I_D/I_G ratio for GO, rGO, and various functionalized (chiral/achiral) rGO. The increase of the I_D/I_G ratio after reduction suggests it is an effective reduction procedure. Figure 2n shows a Fourier Transform Infrared (FTIR) spectrum. The higher intensity shown near the 1000–1100 cm^{-1} region suggests effective chiral/achiral ligand-based loading on the graphite plane. Figure 2o presents a comparison between the NMR spectrums of rGO and various functionalized-rGO inks. A new peak at ≈2.75 ppm is detected, suggesting effective functionalization status of each. Figures 2p and 2q show, respectively, basic field effect transistor (FET) transfer curves and current–voltage (I–V) measurements for rGO sample I–V measurements. The results indicate for n-type FET with Ohmic contact, most probably due to the N$_2$ doping made by the polymer chain of the polydopamine scattering center. Additional information regarding NMR is shown in Supporting Information (Figure S2, Supporting Information).

Figure 2r–w and Figure S3, Supporting Information, show the biocompatibility results of rGOs with various chiral/achiral ligands, which are for the cytotoxic assessment of untreated human lung epithelial cells (BEAS-2B, ATCC, and CRL-9609) after 10–100 µg mL^{-1} treatment for 24 h. The viable cell percentage after treatment has been compared with untreated cells (Figure 2x). Functionalized rGO inks had negligible cytotoxicity

both at low and high concentrations. This assessment could be useful for a continuous production line during fabrication, printing, and measurements regarding par safety issues (see details in Section S3, Supporting Information). The photographs of large-scale printing on paper, porous, and fibrous cellulose from paper substrate are shown in the Figure S4, Supporting Information.

### 2.2. Simultaneous Separation and Recognition of Chiral Molecules

A schematic representation of spatiotemporal separation of chiral molecules using the cellulose-based fibrous and porous cascaded HQS is shown in **Figure 3**a[i]. Due to the presence of an inherent chiral center and the helical shape in the HQS, the incoming enantiomers ((S)- (+)-2-butanol and (R)- (−)-2-butanol)) reach the second layer of the CSEAHQS in a lagging manner and react with the SSD at different timeframes. This causes a divided electrical resistance profile that depends on the nature of spin sensitive/filtering capability as well as various splitting (abundance) profiles of each enantiomer in the mixture from Layer 2; at the time, a superimposed Gaussian-like profile is observed from Layer 1. The specific binding time and release of each handedness from such CSEAHQS at different times from t_0 to t_3 is schematically shown in Figure 3a[i,ii]. Figure 3b–e shows the response pattern to (S)- (+)-2-butanol and (R)- (−)-2-butanol, either as individual components of mixtures with racemic (1:1) and enantiomeric (2:1 and 1:2) ratios, from Layer 2 of the CSEAHQS for different SSDs with typical achiral ligands (e.g., 4-mercaptobenzoic acid (MBZA), 1,4-Phenylenediamine, and diethylamine) and chiral ligands (e.g., 3-mercapto hexanol). SSD with the MBZA shows complete opposite behavior for two different chiral handedness, viz. increase of resistance (up) for S (+) and decrease of resistance (down) for R (−). When compared with the same SSD type (MBZA) in Layer 1 cascade, the sensing profile looks single Gaussian type with no resolving power (see Figure S5, Supporting Information). The other SSDs had either opposite directions or the same directions for individual chiral handedness. Typical data are shown for various cases as per directionality, such as, down–down (1,4-Phenylenediamine in Figure 3c), down–up (diethylamine in Figure 3d), and up–up (3-mercapto hexanol) with related splitting results in the mixture. Each of the splitting profiles is distinct from each other with the presence of a multipeak, suggesting the relative abundance in different time-frames as per transmission rate of each chiral type from Layer 1 to Layer 2, meaning that Layer 2 of the CSEAHQS is more informative than Layer 1 in a racemic/enantiomeric chiral mixture.

To understand the opposite directional changes in chiral S (+)/R (−) exposure, ab initio DFT analyses were conducted for typical SSD case (up–down, Figure 3b of MBZA/polydopamine/rGO (MBZA-PDP-rGO) as sensor-host and S (+) and R (−) butanol as target guests. The optimized structure and HOMO–LUMO gap are shown in Figure 3f–h. Gibbs energy difference (ΔG) of S (+) butanol-MBZA-PDP-rGO and R (−) butanol- MBZA-PDP-rGO complex is −3332.76 and −6.34 kJ mol^{-1}, respectively. The HOMO–LUMO gap of the
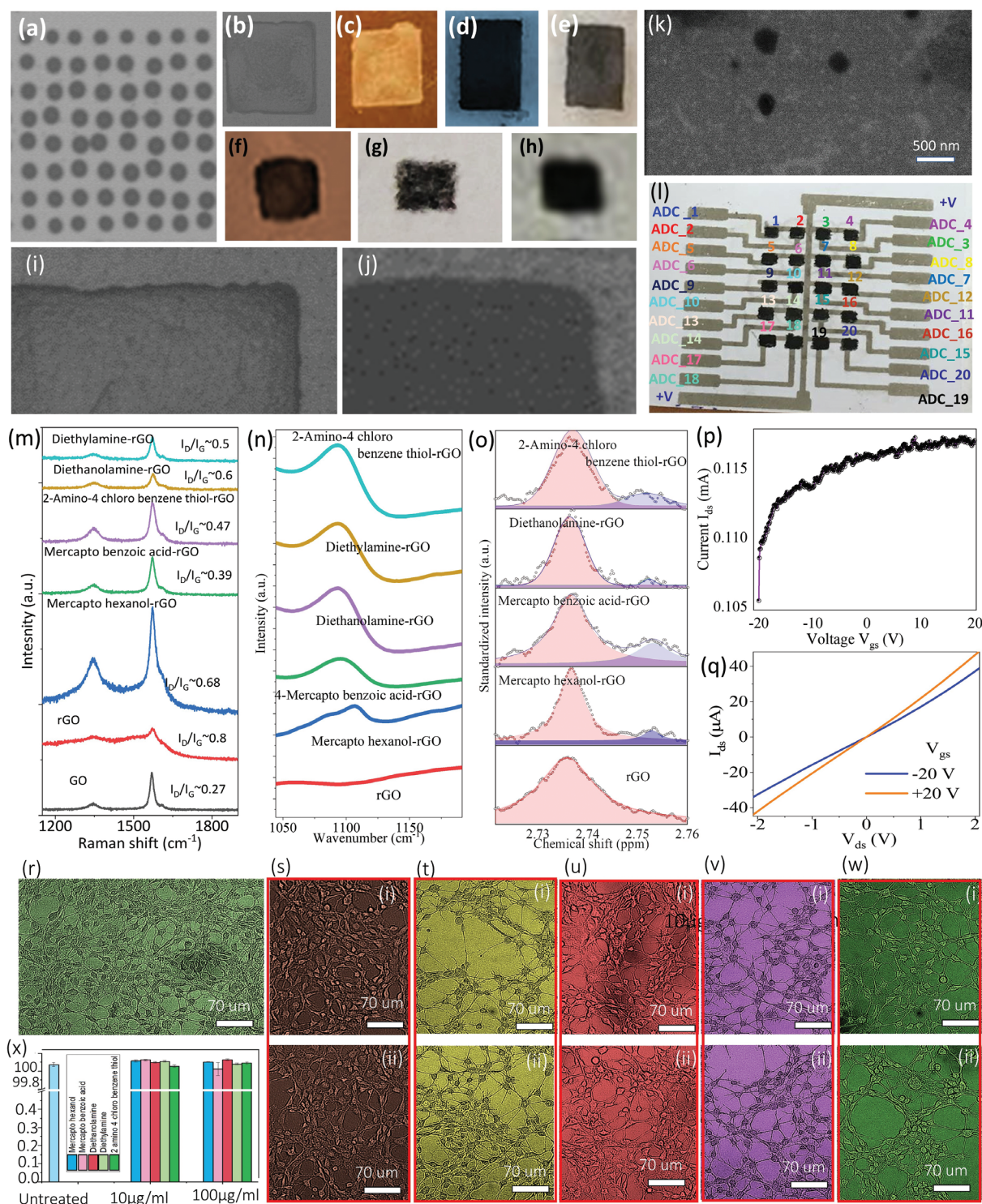
Figure 2. Printing of SSD in various substrate and related characterizations of SSD ink. Inkjet-printed micropixels in the form of matrix for a) 200 µm and b) 60 µm inter-droplet distance (both on an untreated Si/SiO₂ surface). Uniform continuous printed geometrical pattern (typical square and rectangular pattern ≈3 × 3 mm² and ≈3 × 4 mm²) on various rigid and flexible substrates, such as c) Kapton, d) silicone PDMS rubber, e) glass, f) PET, g) filter paper, and h) conventional office printer paper. Magnified image for continuous printed pattern with no "coffee ring effect" on the edge for i) silicon and j) Kapton. k) The SEM microstructure of rGO nano-flex and l) the typical photograph of CSEAHQS with SSD pixels printed on paper. m) Raman, n) FTIR, and o) NMR characteristics of SSD inks. p,q) FET and IV characteristics of rGO. Evaluation of cytotoxicity using human epithelial lung cells (r, untreated) for various SSD inks (thiol, amines, and chiral), such as mercapto hexanol (s (i, ii)), mercapto benzoic acid (t (i, ii)), diethanolamine (u (i, ii)), diethylamine (v (i, ii)), 2-amino-4-chlorobenzoic acid (w (i, ii)) at (i) 10 µg mL⁻¹ and (ii) 100 µg mL⁻¹ dosages, respectively (24 h). x) The live cell percentages for various functionalized-rGO ink concentrations and types of dosage after 24 h treatment.
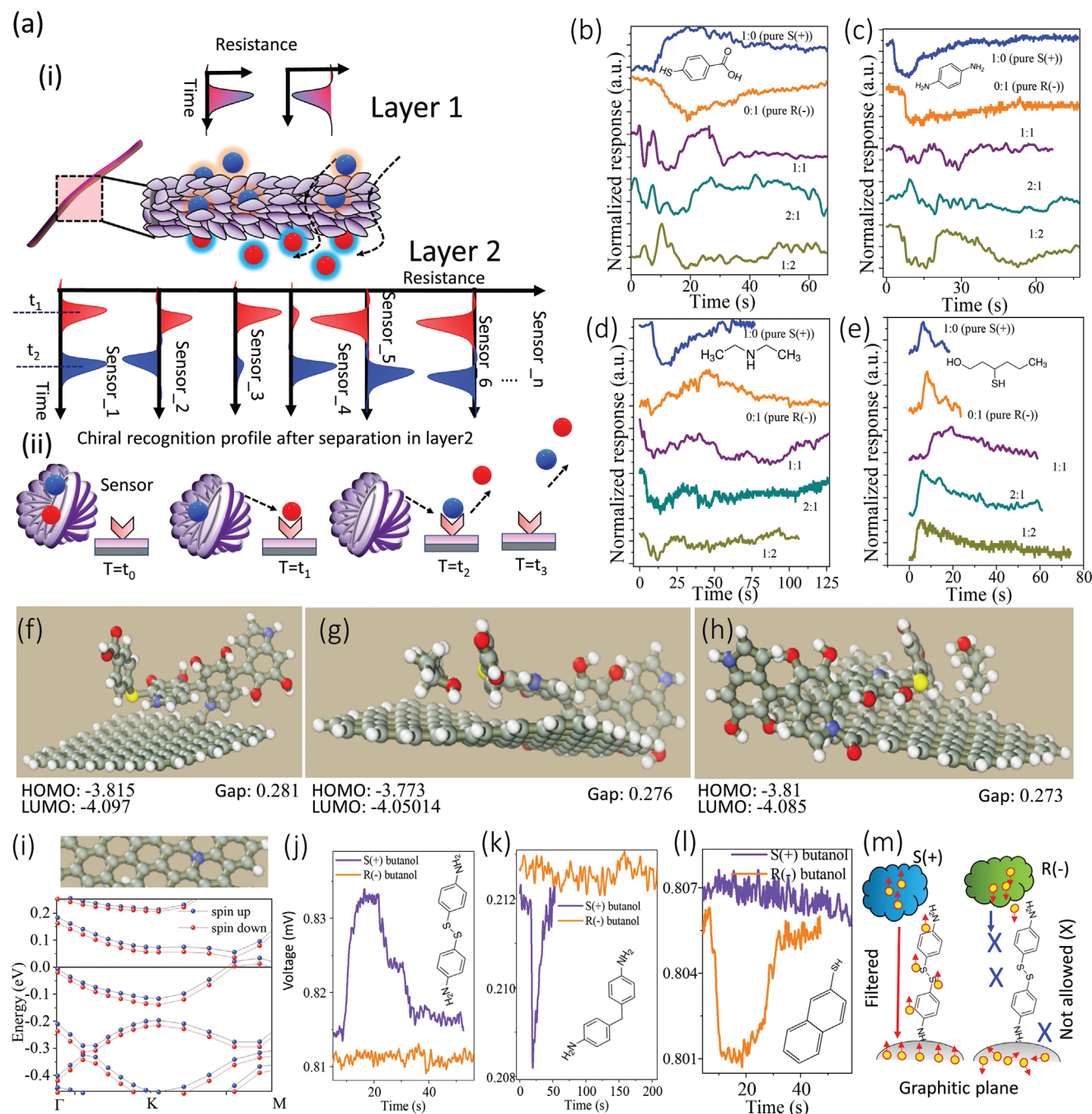
Figure 3. Chiral separation, sensing, and selectivity results, and proposed mechanism. a) Schematic HQS porous architecture for generating splitting resistance profiles in a time-space resolved manner. The sensing results of pure and mixed enantiomers using various SSD with ligands, such as, for b–d) achiral and e) chiral ligands. The optimized structure and calculated HOMO–LUMO for f) polydopamine-rGO, g) S (+) butanol-polydopamine-rGO, and h) R (–) butanol-polydopamine-rGO. i) The spin polarization effect of band gap by N_2 doping at the graphite surface. j–l) Typical chiral selectivity is shown by different other SSD ligands with typical organic spin filter effect (m).

host–guest complex (for S-host and R-host) is calculated as 0.273 and 0.276 eV, respectively, and is lower than that of the host (≈0.281 eV) for both cases. Mullikan charge analyses show that chiral VOC fragments of S (+)/R (–) -butanol- MBZA-PDP-rGO complexes are positive in values, such as, 0.0117 and 0.0137, respectively. This signifies that the butanol fragment for each enantiomer case contributes the charge to the host SSD,

suggesting decreased resistance for each case (same direction). However, that contradicts the real observation of SSD measurements, which has an opposite directional change of electrical resistance.

Pure graphene consisting only of carbon atoms arranged in a hexagonal lattice, is diamagnetic and does not exhibit magnetic behavior. However, when foreign atoms (such as,

H_2, N_2, F) or defects are introduced into the lattice, they break the symmetry of the materials. This phenomenon causes the overlap of p-electron orbitals and creates a magnetic moment in the crystal structure.[30–35] (This is highly desirable for spintronics and chiral recognition. In general, during chiral-based charge transfer, the interaction is also accompanied by spin injection, which is completely opposite to each enantiomer type (CISS). Using this unique spin population, a graphite plane changes markedly its electronic properties (see Figure 1b). This could be attributed to the breaking of local symmetry by N-doping in the C−C lattice during polydopamine encapsulation and reduction of GO to n-type rGO (see schematics in Figure S1, Supporting Information, and n-type FET properties (Figure 2p,q)). The presence of such a scattering center in the 2D lattice in the presence of a specific chiral environment polarizes the channel to a specific spin-state by the Rashba SOI effect and this should be electronically different without the enantiomer (see Figure 2p,q). It will also be different for a different chiral type. The presence of such N_2 scattering center in the 2D lattice in presence of a specific chiral environment polarizes the channel to a specific spin state. This should be electronically different without enantiomers (see Figure 2p,q) and should be opposite for different enantiomer types. To see this effect, DFT band-structure calculation using opposite spin population ($<\uparrow$ or $<\downarrow$) on N_2 incorporated graphene was done. Figure 3i shows distinct band modulation plot for each type (blue: spin up [$E_g = 0.085$ eV] and red: spin down [$E_g = 0.069$ eV]). This opposite band adjustments due to CISS-assisted opposite spin population could be the reason for reverse resistance changes for each chiral handedness.

MSSA receivers on the graphitic lattice could also act as a coherent spin channel, so that specific spin from the enantiomer could reach to the graphitic lattice without losing primary spin information. These results are in alignment with previous theoretical and experimental studies that showed the ability of various ligands (e.g., thiol [−SH], thiolates [−S], amidine [−NH_2], and carboxylic-acids [–COOH]) to serve as frontier orbitals with larger spin relaxation length due to small SOI even at room temperature.[36–38] Other studies have shown that ferromagnetic lead (spin injector) coupled with such organic linkers (spin channel/filter) indicate coherent spin transmission capability.[39] This fascinating result seems highly practical in our case; yet, instead of using a ferromagnet, the spin injection source consists of chiral molecules in one end, while their relative effect is felt at the other end of the functionalized graphite lattice. Figure 3j–l shows such selective chiral response for various other SSDs with different ligand types. The schematic representation for a specific chiral filter type is shown in Figure 3m. One similarity for these three cases is that each of the ligand types has two consecutive benzene rings in their structure.

To evaluate the chirality resolving power of CSP through splitting resistance profile of enantiomeric mixture, molecular modeling simulation was used to show the binding affinity between cellulose and each vapor type of an enantiomer with defined chiral center. The calculated energies for cellulose-S (+) butanol and cellulose-R (−) butanol complex were −146 113.24 and −146 112.25 kcal mol^{-1}, respectively, suggesting an asymmetry in the binding energy that cause difference in the releasing time for each enantiomer type while passing

through hairy fibrous network (from first layer to second). The experimental evidence for the separation capability of helical cellulose fibers for different enantiomers has been reported elsewhere.[40] The typical separation factor, retention factor, and resolution for racemic mixtures of S (+) butanol and R (−) butanol are shown in Figure S6, Supporting Information, using typical ligand 1,4-Phenylenediamine- as a SSD concerning the direction resistance change of each enantiomer type. The fitting results to evaluate such parameters for opposite directional resistance movement of current in chiral exposure for other ligands are problematic due to overlap issues. To counteract this issue, and for automated estimation of the components of chiral molecules in the mixture, a synthetic image-based classification was carried out based on such splitting responses of all SSD types and deep learning-based model for automated classifications and quantifications of different chiral mixtures (see Section 2.3).
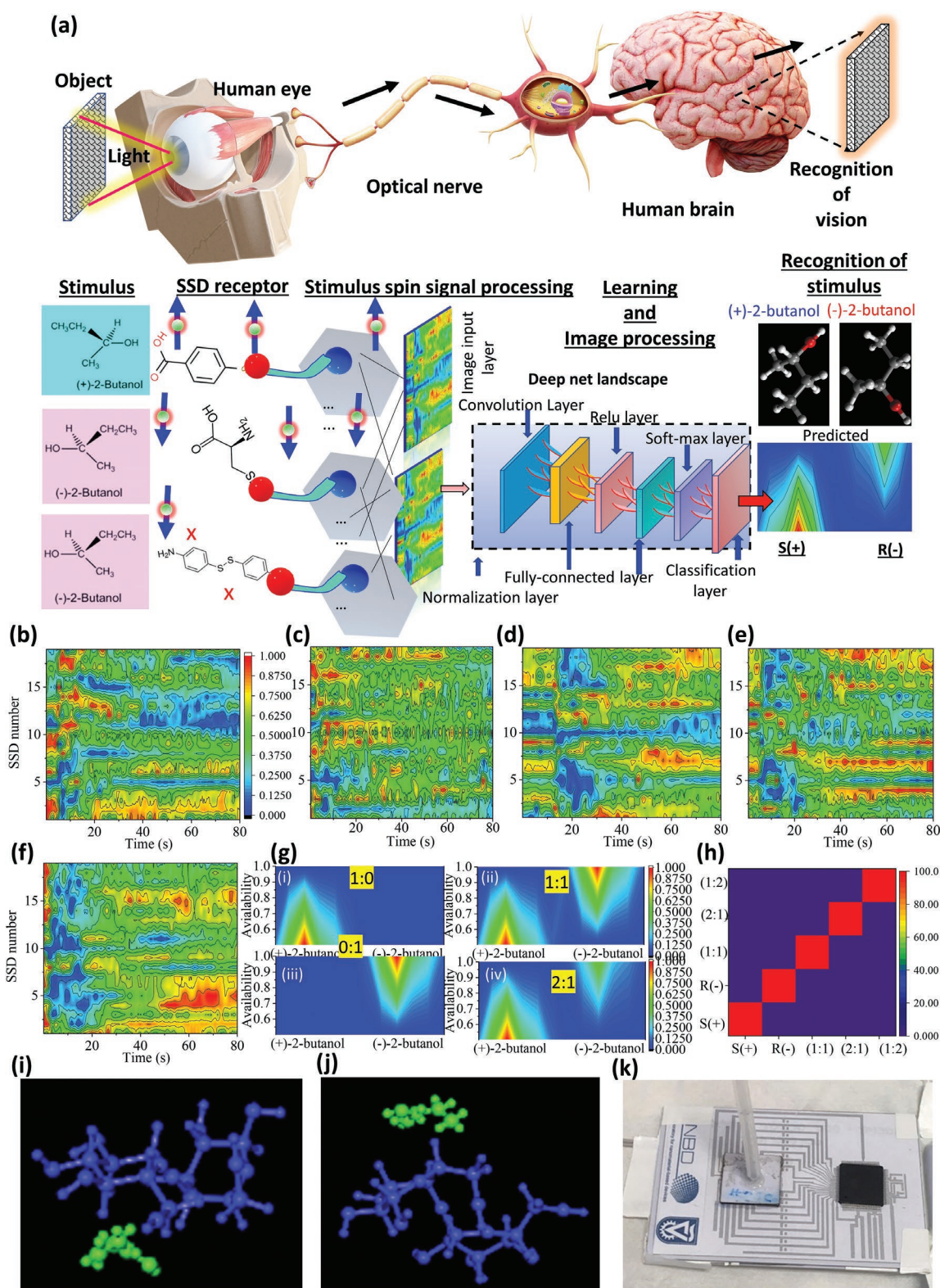
2.3. Neuromorphic Vision Synthetic Imaging of Spin-Pumping to SSD Receptors

To extract the automated features and for continuous estimation of each chiral type in the mixture automatically from such a splitted resistance profile from each SSD, a synthetic image processing technique and a deep neural network-based self-learning architecture was tested.

Layer 2 of CSEAHQS-based SSD detectors was used to construct synthetic image profile for pure enantiomers and their mixture via a bio-inspired neuromorphic human vision (**Figure 4**a) and neuromorphic spintronics.[41,42] Figure 4b–f shows a typical image quality as seen by the combined influence from each SSD. The images show distinct patterns bearing the influence of MSSA chemistry, inter-SSD dependence, and spatiotemporal splitting information by HQS in one image (see demonstration Videos S1 and S2, Supporting Information). These composite images were then used for a deep-net system for self-learning architecture as input, with systematic training and the relative chiral concentration ratio being evaluated with color coding (Figure 4g) for a real-time view for industrial production line and classification accuracy (>95%) shown in a confusion matrix with relevant color coding (Figure 4h). Figure 4k shows the photograph of a chiral micro-spectrometer embedded with a microprocessor-based computing unit, bi-layer printed SSDs, and inlet/outlet.

The reported CSEAHQS system was also tested upon exposure to other chiral enantiomer vapors, such as limonene (+ and −) and their mixtures (racemic and enantiomeric). The difference between the two enantiomers of limonene (S-limonene and R-limonene) as supplied is their chiral handedness with distinct properties, such as a completely different smell. Enantiomer (R)- has the characteristic smell of oranges, whereas the (S)- smells like lemons. The SSD generated image patterns for pure (1:0 and 0:1) and mixtures (2:1, 1:1, 1:2) of these enantiomers are shown in Figure S7a–e, Supporting Information, and are unique in each case. The calculated energy of cellulose-S-limonene and cellulose-R-limonene was −158 107.92 and −158 081 kcal mol^{-1}, respectively. This represents asymmetry in a binding energy with HQS while forming the complex during their passage from one layer to

Figure 4. A neuromorphic vision inspired deep-learning architecture for SSD signal processing from spin pumping. a) Spin transfer dynamics signal processing to generate a synthetic image using SSDs for various enantiomer as spin injector (stimulus) in one end and the effect is reflected at the other side (graphite network) for generating synthetic image, deep net image processing, learning, and predictions of different mixed enantiomers. The synthetic image generated for pure b) S (+)-butanol, c) R (−) butanol, and their mixtures for d–f) 1:1, 2:1, and 1:2. The predicted results from deep neural network are shown in (g) and (h). The optimized structure for enantiomer-cellulose for: i) cellulose-S (+)-butanol, and j) cellulose-R (−) butanol. k) Photograph of chiral spectrometer embedded with micro-controller and inlet–outlet.
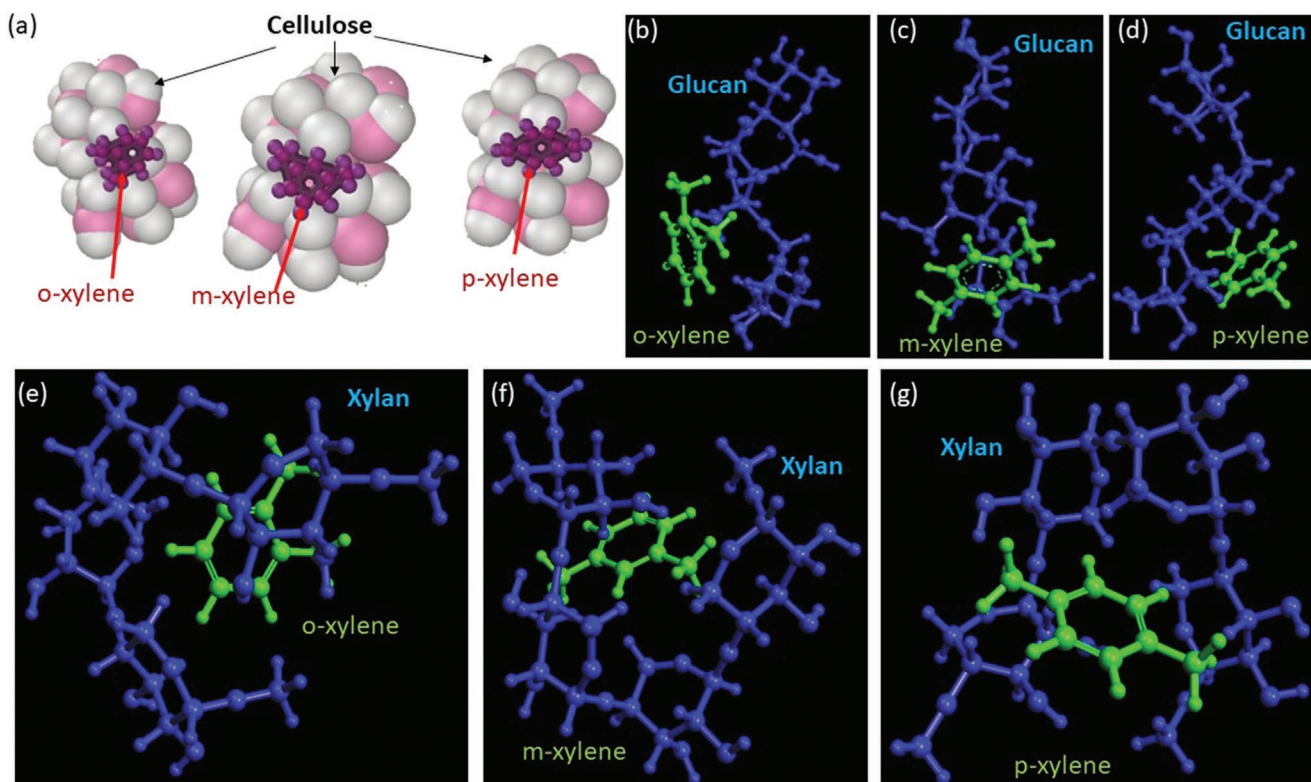
Figure 5. Molecular dynamic simulation results of various CSP components of papers with xylene isomers. The optimized structure for major helical fibers, such as a) xylene isomer-cellulose and other minor components, b-d) xylene isomer-glucan, and e-g) xylene isomer-xylan.

next. The optimized geometries of each complex are shown in Figure S7f,g, Supporting Information.

2.4. Sensing Study of Mixed Isomers

The present system was also tested for isomer sensing of xylene (*ortho, meta, para*) for pure samples and various mixtures of them (*o:m:p* = 1:1:1, 2:1:1, 1:2:1, 1:1:2). The typical image pattern is shown in Section S8 and Figure S8a–h, Supporting Information. The relevant classification result is shown in Figure S8i, Supporting Information. The figures indicate that the reported CSEAHQS could also be used for isomer sensing for individual and mixed samples. The major reason for the splitted sensing profile could be related to the asymmetry in the binding energy of isomers with the components of papers, for example, predominantly with cellulose (see the optimized structures in **Figure 5**a). Other small amounts of components such as xylan and glucan could influence some amounts in mass transfer rate and isomeric elution as well (the optimized structures are shown in Figure 5b–d for glucan-isomers [*o,m,p*] and Figure 5e–g for xylan-isomers [*o,m,p*]). The calculated energy of each of the complexes is different to the other and is tabulated in Table S1, Supporting Information.

2.5. Possible Applications of CARE Phenomena, MSSA, and CSEAHQS

As mentioned above, CARE phenomena express a polarized scattering when a chiral molecule is adsorbed on the SSD surface. In contrast to conventional unpolarized scatterers (e.g., hydrogen and heavy gas atoms adsorbed on 2D graphite lattice), the CARE-controlled spin modulation source can be used for maintaining long-term coherence. This could be attributed to the CISS-pumped spin specificity and MSSA-based spin filtering when the surface is bombarded with chiral gas molecules. In this configuration, chiral exposure could affect the entire channel with specific spin types, leading to an opposite resistance change for two different enantiomers that are adsorbed on the specific SSD. In this context, it has to be clarified whether the experimental demonstration of spin coherence time is problematic, because the injected enantiomer molecules come, react, and leave the SSD (like a pulse) due to the continuous dynamic flow from one layer to another (HQS's hierarchical structures). Exposing the SSD to a constant chiral atmosphere could enable the efficient utilization of the CARE-controlled organic-inorganic CSEA hybrid approach. Another advantage of the CISS-powered CSEA hybrid device is that it does not necessarily need a third electrode (gate-control of spin) nor the ferromagnetic electrode (spin injection ports)/ high voltage, like the conventional spin transistor type,[43] as the implanted organic MSSA filters on graphite lattice can transfer a spin polarized electron to the channel. Conventional spintronic devices need permanent ferromagnetic electrodes and are problematic for miniatured nanoscale spintronics because ferromagnetic materials behave super-paramagnetically at nano-dimensions. However, the present MSSA-based approach could be applicable for conventional non-magnetic electrodes with no issue for miniaturization. Therefore, this could be highly useful for developing quantum electronics, low-power

magnet free-spintronics, and fundamental device components of quantum computing at room temperature. Nevertheless, the reported cascaded architecture of the porous HQS sensing system could be utilized for other mixed gas sensing applications with a simultaneous separation and recognition, by increasing sensor-printed paper layers, paper quality, and thickness of a specific paper grade. This will be highly important for drug research and molecular spectroscopy-based clinical diagnosis of diseases of the skin, breath, blood, cancer tumor recognition, etc.[44,45]

3. Summary and Conclusions

We have reported on the design of a spin-controlled spectrometer using binder-free printed hybrid graphene-based SSDs, coupled with a cellulose-based helical sieving effect (HQS) in CSEAHQS architecture. The proposed system shows simultaneous chiral recognition and chiral separation of a variety of mixed chiral organic molecules, such as butanol (+ and −) and limonene (+ and −). Chiral recognition is achieved by CISS-assisted spin injection from specific enantiomers and received through a MSSA-based implanted ligand on the graphite plane and CARE, which is generated by an effective magnetic field on the moving charge inside the 2D lattice through a relativistic effect. It proved advantageous to use a magnet-free approach for chiral spectroscopy compared to other magnetic resonance-based spectroscopy, such as NMR/ESR. Due to the small SOI and negligible hyperfine interaction specific ligands at some SSDs, chiral selectivity was found by allowing specific spin-types (spin filtering). Chiral separation was observed by the splitted resistance profile, caused by asymmetry in the binding energies between the HQS phase and enantiomers. This is highly useful for generating a unique synthetic image pattern and can be later used for estimation of chiral mixtures or isomer mixers with a neuromorphic vision inspired deep-learning architecture. The proposed miniatured SSD spectrometer design, along with an AI supported automated analyzing system, could be useful in the rapid detection of drugs, chiral spintronics, and other automated industrial process optimizations. CARE phenomena and MSSA-based spin pumping/filtering could be used for magnet-free nano-scale 2D spintronics, a gate-free spin-controlled device, as well as room temperature spintronics and quantum computing.

4. Experimental Section

Binder-Free Inkjet Printing Recipe for Functionalized Graphene Ink: The dried functionalized hybrid rGO powders modified with a selection of chiral and achiral ligands was redispersed in DMF and sonicated at low power for ≈1–2 min to disperse the ink that was subsequently used for inkjet printing (Dispensing system with piezoelectric nozzle [Scienion, model sciFLEXARRAYER S3]) on paper for preparing the SSDs. Details of the synthesis, binder-free print approach, printing on a wide range of substrates, reaction mechanism, and list of biochemical ligands (thiols, amines, chiral compounds) are discussed in Section 1. The silver nanowires-based electrodes were used for connecting multi-SSDs. Details of the synthesis procedure is provided in Section 3.

Surface Characterizations: A morphological study using SEM (Sigma 500, Zeiss Ultra-Plus High-Resolution SEM, Germany) gave a microscopic view of the synthesized materials dispersed in alcohol and spin-coated on silicon wafers (Si/SiO$_2$) to distribute the flakes uniformly. Images were acquired at ≈5 kV electron acceleration and 4–8 mm working distances. Raman spectra (Horiba Jobin Yvon LabRAM HR Evolution Micro-Raman, Japan) were obtained with a 532 nm laser. All samples dispersed in ethanol were spin-coated on silicon wafers and dried overnight in a vacuum chamber before measurements were taken. For FTIR (Bruker Vertex 70 V KBr BS vertical ATR-FTIR, USA) measurements (300–4000 cm^{-1}), the cleaned and overnight-dried sample powder was mixed with KBr to form a pellet. ^{1}H NMR analysis was done with a Bruker AV-III400 MHz 2-channel spectrometer with direct detection probe based with automatic tuning and matching (equipped with z gradients) at room temperature, using ≈500 µL d-DMSO (Sigma Aldrich, USA) as the solvent at 30 °C, a ^{1}H pulse with 1 s repetitions.

Electrical Characterization: For typical gate-dependent FET properties[18,46,47,50,51] to determine the carrier type, functionalized rGO samples were spin-coated on Si/SiO$_2$ wafers with an electrometer (Keithley 2636A and 3706, USA) interfaced with Labview software, USA.

Cell Culture Treatment with Functionalized rGO Inks to Assess Cytotoxicity: Human epithelial lung cells (BEAS-2B, ATCC, CRL-9609, Israel) were seeded at 96×10^3 per well on 24-well plates and cultured with 0.5 mL full Roswell Park Memorial Institute (RPMI)-1640 medium (Sigma-Aldrich, Israel) at 37 °C with 5% CO$_2$ in air. After 24 h recovery, the cells were washed with phosphate buffered saline (PBS) Ca^{2+}/Mg^{2+} (Sigma-Aldrich, Israel) and the treatments were applied for 24 h in the culture medium. Hybrid rGO samples were cleaned with ethanol and dried overnight before cell culture. The typical hybrid rGO powder samples containing different thiol/amine-based chiral/achiral ligands, such as mercapto hexanol, mercapto benzoic acid, diethanolamine and diethylamine, and 2-amino-4-chloro-benzene thiol were vortexed with RPMI 1640 at 10 and 100 µg mL^{-1}. The cells were then exposed to each hybrid rGO sample from ≈10 to 100 µg mL^{-1} for 24 h. The experiment on an animal model using functionalized rGO could be found elsewhere.[48]

Annexin V–FITC/Propidium Iodide Assay: After 24 h treatment at the indicated concentrations, cells were gently washed with PBS. Annexin-V and propidium iodide staining was used (BioLegend, California, US) at 0.2 mL RPMI-1640 medium per well. The cells were gently washed with PBS and 0.2 µg mL^{-1} Hoechst 33342 solution (Invitrogen by Thermo-Fisher Scientific, Israel) was added. The cells were analyzed using an In Cell Analyzer 2000 System (Technion Life Sciences and Engineering Infrastructure Center, Technion, Israel). For details, see Section S3, Supporting Information.

DFT and Molecular Modeling: Gaussian 16 software was used to optimize the molecular structure as well as the HOMO and LUMO energy of polydopamine-rGO, (g) S (+) butanol-polydopamine-rGO, and (h) R (−) butanol-polydopamine-rGO, and also their complexes R- and S-2-butanol molecules using a DFT method with Austin–Frisch–Petersson functional with dispersion (APFD) and the basis set 6-31G (d). APFD, including treatments of the dispersion effects, represented the best trade-off between accuracy and computational cost for a relatively large system.[49] After relaxing the geometry of the host (cellulose) and the target (enantiomer), a docking simulation (generally followed for protein-ligand binding calculation) was used for finding the lowest energy position to measure molecular dynamic simulation. The typical boundary of the simulation box was set as $45 \times 45 \times 45$ Grid size with a resolution of 0.4 Å in a flexible mode. The maximum number of the host guest pose was set at 5000 to find the suitable position for binding. Ab initio quantum DFT analysis for electronic structure and spin-dependent band gap calculations was carried out for the iterative solution of the Kohn–Sham equation in a plane-wave set with ultrasoft pseudopotentials. Here the Perdew–Burke–Ernzerhof exchange-correlation functional of the generalized gradient approximation was used. The plane-wave cutoff for wave function was set at 597 eV. The graphene sheets were separated by ≈20 Å along a perpendicular direction to avoid interlayer influence. The Brillouin zone was sampled with the Monkhorst–Pack scheme with a 7x7x1 k-mesh in Gaussian smearing condition. Spin polarization involved replacing one carbon atom with N by setting the 100% spin up/down configuration at the N site.

Deep Neural Network and Image Processing: For the enantiomers' mix state, image processing by a synthetically constructed input image from Layer 2 HSGC data was used, which was fed to the self-learning architecture of deep-net layers that had the following consecutive layers, such as image-input layer, convolution2dLayer, reluLayer, maxPooling2dLayer, fully connected layer, and classification layers. Before training, each image input sequence was resized with the same dimension. Deep net system automatically sampled the features from the image by itself, and was used for learning to classify the mixed enantiomers and isomers.Acknowledgements

Conflict of Interest

The authors declare no conflict of interest.

Data Availability Statement

The data that support the findings of this study are available in the supplementary material of this article.

Supporting Information

Supporting Information is available from the Wiley Online Library or from the author.

[1] L. D. Barron, in *Chirality at the Nanoscale: Nanoparticles, Surfaces, Materials and More*, Vol. *1*, (Eds: D. B. Amabilino), Wiley-VCH, Germany **2009**, Ch. 1.

[2] J. V. Brakel, in *Philosophy of Chemistry*, Vol. *6*, (Eds: A. I. Woody, R. F. Hendry, P. Needham), Elsevier, North Holland **2012**, Ch. 18.

[3] W. D. Lubell, K. S. Beauregard, F. Polyak, in *Comprehensive Chirality*, Vol. *1*, (Eds: H. Yamamoto, E. M. Carreira), Elsevier, North Holland **2012**, Ch. 1.6.

[4] D. R. Gere, *Science* **1983**, *222*, 253.

[5] G. Kucerova, K. Kalikova, E. Tesarova, *Chirality* **2017**, *29*, 239.

[6] T. Tozawa, J. T. A. Jones, S. I. Swamy, S. Jiang, D. J. Adams, S. Shakespeare, R. Clowes, D. Bradshaw, T. Hasell, S. Y. Chong, C. Tang, S. Thompson, J. Parker, A. Trewin, J. Bacsa, A. M. Z. Slawin, A. Steiner, A. I. Cooper, *Nat. Mater.* **2009**, *8*, 973.

[7] M. L. Lee, K. E. Markides, *Nature* **1987**, *327*, 441.

[8] E. Hendry, T. Carpy, J. Johnston, M. Popland, R. V. Mikhaylovskiy, A. J. Lapthorn, S. M. Kelly, L. D. Barron, N. Gadegaard, M. Kadodwala, *Nat. Nanotechnol.* **2010**, *5*, 783.

[9] L. Chen, P. S. Reiss, S. Y. Chong, D. Holden, K. E. Jelfs, T. Hasell, M. A. Little, A. Kewley, M. E. Briggs, A. Stephenson, K. M. Thomas, J. A. Armstrong, J. Bell, J. Busto, R. Noel, J. Liu, D. M. Strachan, P. K. Thallapally, A. I. Cooper, *Nat. Mater.* **2014**, *13*, 954.

[10] P. L. Polavarapu, J. He, *Anal. Chem.* **2004**, *76*, 61 A.

[11] L. Torsi, G. M. Farinola, F. Marinelli, M. C. Tanese, O. H. Omar, L. Valli, F. Babudri, F. Palmisano, P. G. Zambonin, F. Naso, *Nat. Mater.* **2008**, *7*, 412.

[12] X. Shang, I. Song, H. Ohtsu, Y. H. Lee, T. Zhao, T. Kojima, J. H. Jung, M. Kawano, J. H. Oh, *Adv. Mater.* **2017**, *29*, 1605828.

[13] L. Wang, W. Gao, S. Ng, M. Pumera, *Anal. Chem.* **2021**, *93*, 5277.

[14] N. J. Kyber, M. B. Lerner, J. S. Yodh, G. Preti, A. T. C. Johnson, *ACS Nano* **2013**, *7*, 2800.

[15] N. M. Maier, P. Franco, W. Lindner, *J. Chromatogr. A* **2001**, *906*, 3.

[16] S. Inagaki, J. Z. Min, T. Toyo'oka, *Anal. Chem.* **2008**, *80*, 1824.

[17] A. Hierlemann, H. Baltes, V. Schurig, *Enantiomer* **2001**, *6*, 129.

[18] A. Maity, S. Rapoport, H. Haick, *Small* **2022**, e2205038.

[19] B. Göhler, V. Hamelbeck, T. Z. Markus, M. Kettner, G. F. Hanne, Z. Vager, R. Naaman, A. H. Zacharias, *Science* **2011**, *331*, 894.

[20] X. Yang, C. H. van der Wal, B. J. van Wees, *Phys. Rev. B* **2019**, *99*, 024418.

[21] C. D. Aiello, J. M. Abendroth, M. Abbas, A. Afanasev, S. Agarwal, A. S. Banerjee, D. N. Beratan, J. N. Belling, B. Berche, A. Botana, J. R. Caram, G. L. Celardo, G. Cuniberti, A. Garcia-Etxarri, A. Dianat, I. Diez-Perez, Y. Guo, R. Gutierrez, C. Herrmann, J. Hihath, S. Kale, P. Kurian, Y.-C. Lai, T. Liu, A. Lopez, E. Medina, V. Mujica, R. Naaman, M. Noormandipour, J. L. Palma, et al., *ACS Nano* **2022**, *16*, 4989.

[22] Z. Xie, T. Z. Markus, S. R. Cohen, Z. Vager, R. Gutierrez, R. Naaman, *Nano Lett.* **2011**, *11*, 4652.

[23] R. A. Rosenberg, D. Mishra, R. Naaman, *Angew. Chem.* **2015**, *54*, 7295.

[24] M. Kettner, B. Göhler, H. Zacharias, D. Mishra, V. Kiran, R. Naaman, C. Fontanesi, D. H. Waldeck, S. Sęk, J. Pawłowski, J. Juhaniewicz, *J. Phys. Chem. C* **2015**, *119*, 14542.

[25] R. Naaman, D. H. Waldeck, *Annu. Rev. Phys. Chem.* **2015**, *66*, 263.

[26] V. Dediu, M. Murgia, F. C. Matacotta, C. Taliani, S. Barbanera, *Solid State Commun.* **2002**, *122*, 181.

[27] Z. H. Xiong, D. Wu, Z. V. Vardeny, J. Shi, *Nature* **2004**, *427*, 821.

[28] J. H. Shim, K. V. Raman, Y. J. Park, T. S. Santos, G. X. Miao, B. Satpati, J. S. Moodera, *Phys. Rev. Lett.* **2008**, *100*, 226603.

[29] X. Zhang, S. Mizukami, T. Kubota, Q. Ma, M. Oogane, H. Naganuma, Y. Ando, T. Miyazaki, *Nat. Commun.* **2013**, *4*, 1392.

[30] K. M. McCreary, A. G. Swartz, W. Han, J. Fabian, R. K. Kawakami, *Phys. Rev. Lett.* **2012**, *109*, 186604.

[31] A. J. Giesbers, K. Uhlířová, M. Konečný, E. C. Peters, M. Burghard, J. Aarts, C. F. J. Flipse, *Phys. Rev. Lett.* **2013**, *111*, 166101.

[32] D. W. Boukhvalov, M. I. Katsnelson, A. I. Lichtenstein, *Phys. Rev. B* **2008**, *77*, 035427.

[33] X. Hong, K. Zou, B. Wang, S. H. Cheng, J. Zhu, *Phys. Rev. Lett.* **2012**, *108*, 226602.

[34] E. J. G. Santos, D. Sánchez-Portal, A. Ayuela, *Phys. Rev. B* **2010**, *81*, 125433.

[35] H. Zhang, C. Lazo, S. Blügel, S. Heinze, Y. Mokrousov, *Phys. Rev. Lett.* **2012**, *108*, 056802.

[36] F. Chen, X. Li, J. Hihath, Z. Huang, N. Tao, *J. Am. Chem. Soc.* **2006**, *128*, 15874.

[37] L. Venkataraman, J. E. Klare, I. W. Tam, C. Nuckolls, M. S. Hybertsen, M. L. Steigerwald, *Nano Lett.* **2006**, *6*, 458.

**ADVANCED
SCIENCE NEWS**

www.advancedsciencenews.com

**ADVANCED
MATERIALS**

www.advmat.de

[38] R. Farzadi, H. M. Moghaddam, D. Farmanzadeh, *Chem. Phys. Lett.* **2018**, *704*, 37.

[39] S. Lach, A. Altenhof, K. Tarafder, F. Schmitt, E. Ali, M. Vogel, J. Sauther, P. M. Oppeneer, C. Ziegler, *Adv. Funct. Mater.* **2012**, *22*, 989.

[40] Y. Katoh, Y. Tsujimoto, C. Yamamoto, T. Ikai, M. Kamigaito, Y. Okamoto, *Polym. J.* **2011**, *43*, 84.

[41] J. Grollier, D. Querlioz, K. Y. Camsari, K. Everschor-Sitte, S. Fukami, M. D. Stiles, *Nat. Electron.* **2020**, *3*, 360.

[42] F. Zhou, Z. Zhou, J. Chen, T. H. Choy, J. Wang, N. Zhang, Z. Lin, S. Yu, J. Kang, H.-S. P. Wong, Y. Chai, *Nat. Nanotechnol.* **2019**, *14*, 776.

[43] S. Datta, B. Das, *Appl. Phys. Lett.* **1990**, *56*, 665.

[44] G. Peng, U. Tisch, O. Adams, M. Hakim, N. Shehada, Y. Y. Broza, S. Billan, R. A. Bortnyak, A. Kuten, H. Haick, *Nat. Nanotechnol.* **2009**, *4*, 669.

[45] A. Maity, Y. Milyutin, V. D. Maidantchik, Y. H. Pollak, Y. Broza, R. Omar, Y. Zheng, W. Saliba, T.-P. Huynh, H. Haick, *Adv. Sci.* **2022**, *9*, 2203693.

[46] A. Shalabny, F. Buonocore, M. Celino, G. Shalev, L. Zhang, W. Wu, P. Li, J. Arbiol, M. Y. Bashouti, *Nano Lett.* **2020**, *20*, 8369.

[47] M. Khatib, H. Haick, *ACS Nano* **2022**, *16*, 7080.

[48] M. Zhang, J. J. Sun, M. Khatib, Z. Lin, Z. Chen, W. Saliba, A. Gharra, Y. D. Horev, V. Kloper, Y. Milyutin, T. P. Huynh, S. Brandon, G. Shi, H. Haick, *Nat. Commun.* **2019**, *10*, 1120.

[49] A. Shalabny, F. Buonocore, M. Celino, L. Zhang, K. Sardashti, M. Härth, D. W. Schubert, M. Y. Bashout, *Appl. Surf. Sci.* **2022**, *599*, 153957.

[50] A. Maity, X. Sui, B. Jin, H. Pu, K. J. Bottum, X. Huang, J. Chang, G. Zhou, G. Lu, J. Chen, *Anal. Chem.* **2018**, *90*, 14230.

[51] A. Maity, X. Sui, H. Pu, K. J. Bottum, B. Jin, J. Chang, G. Zhou, G. Lu, J. Chen, *Nanoscale* **2020**, *12*, 1500.